



**HAL**  
open science

## Identification of a set of macroscopic elastic parameters in a 3D woven composite: Uncertainty analysis and regularization

R Gras, H Leclerc, F Hild, Stéphane Roux, Julien Schneider

► **To cite this version:**

R Gras, H Leclerc, F Hild, Stéphane Roux, Julien Schneider. Identification of a set of macroscopic elastic parameters in a 3D woven composite: Uncertainty analysis and regularization. *International Journal of Solids and Structures*, 2015, 55, pp.2-16. 10.1016/j.ijstr.2013.12.023 . hal-01166765

**HAL Id: hal-01166765**

**<https://hal.science/hal-01166765>**

Submitted on 23 Jun 2015

**HAL** is a multi-disciplinary open access archive for the deposit and dissemination of scientific research documents, whether they are published or not. The documents may come from teaching and research institutions in France or abroad, or from public or private research centers.

L'archive ouverte pluridisciplinaire **HAL**, est destinée au dépôt et à la diffusion de documents scientifiques de niveau recherche, publiés ou non, émanant des établissements d'enseignement et de recherche français ou étrangers, des laboratoires publics ou privés.

# Identification of a set of macroscopic elastic parameters in a 3D woven composite: Uncertainty analysis and regularization

R. Gras<sup>a,b,c</sup>, H. Leclerc<sup>a</sup>, F. Hild<sup>a</sup>, S. Roux<sup>a</sup>, J. Schneider<sup>b</sup>

<sup>a</sup>*LMT Cachan, ENS-Cachan / CNRS / UPMC / PRES UniverSud Paris,  
61, Avenue du Président Wilson, 94235 Cachan Cedex, France*

<sup>b</sup>*Snecma Villaroche - Rond Point René Ravaut  
Réau 77550 Moissy-Cramayel, France*

<sup>c</sup>*now at COHMAS Lab  
4700 King Abdullah University of Science and Technology  
Thuwal 23955-6900, Kingdom of Saudi Arabia*

---

## Abstract

Performing a single but complex mechanical test on small structures rather than on coupons to probe multiple strain states / histories for identification purposes is nowadays possible thanks to full-field measurements. The aim is to identify many parameters thanks to the heterogeneity of mechanical fields. Such an approach is followed herein, focusing on a blade root made of 3D woven composite. The performed test, which is analyzed using global digital image correlation, provides heterogeneous kinematic fields due to the particular shape of the sample. This displacement field is further processed to identify the four in-plane material parameters of the macroscopic equivalent orthotropic behavior. The key point, which may limit the ability to draw reliable conclusions, is the presence of acquisition noise in the original images that has to be tracked along the DIC / identification processing to provide uncertainties on the identified parameters. A further regularization based on *a priori* knowledge is finally introduced to compensate for possible lack of experimental information needed for completing the identification.

*Keywords:* Anisotropy, Digital Image Correlation, elastic material, finite elements, mechanical testing

---

## 1. Introduction

Composite materials are more and more employed in the aeronautical and aerospace industries due to their attractive specific mechanical properties. Recently, the development of 3D woven composites prompted their use in new applications requiring high mechanical properties such as the engine fan blade [1]. Compared to layered architectures where delamination is one of the major failure mode, 3D woven composites are strengthened by tow weaving patterns [2]. However, the principle of weaving induces more waviness in the material and hence the gain of strength on the out-of-plane direction results in strength loss along in-plane directions [3]. The fabrication process has been studied to optimize the position and orientation of the tows in the preform, and to design an injection route compatible with the fabric geometry limiting void generation [4, 5, 6]. Based upon these different works, the process is well

understood and mastered, and it now allows for the design of fabric geometries that are tailored to a given component part with a large flexibility to accommodate for arbitrary geometry and loading conditions.

From the knowledge of the mesostructure and its mechanical properties [7], the elastic behavior of such materials can be modeled based on the homogenization theory [8, 9, 10]. Yet, experimental validation remains a challenge both for validating the present fabrication of crucial parts, and for the design of new ones. The object of this study is to identify material parameters of a 3D woven composite from data extracted from a specific test on a blade dovetail root. An improved identification methodology is proposed to incorporate *a priori* knowledge in a Tikhonov regularization framework. Such regularization, which is described in Ref. [11], has been applied to the detection of damage [12]. It is shown that the Tikhonov regularization acts as a gradual filter on the smaller singular values of the inverse problem. A comparable regularization exploiting the homogenized value of the identified material parameter has been utilized [13]. Regularization of the identification problem based on space reduction through closed-form solutions to the mechanical problem [14], or through the extraction of the statically admissible stress fields from the measured kinematic data [15] have also been developed. It is proposed herein to scale the level of regularization based on the uncertainty of the *a priori* knowledge. Hence, the uncertainty on the identified material parameters due to the CCD sensor noise is estimated. It is the aim of the present study to investigate the combination of full field kinematic measurements in conjunction with numerical modeling to assess a physically and mechanically reliable modeling.

The material, the specimen geometry and the mechanical test are described in Section 2. The identification method is based on the finite element (FE) model introduced in Section 3, and on two-dimensional full-field measurements obtained through *global* Digital Image Correlation (DIC) summarized in Section 4.1. Section 4.2 explains the algorithm for FE model updating and implementation details are given in Section 4.3. Last, Section 5 deals with the results obtained on the studied material and the corresponding uncertainties induced by picture acquisition noise.

## **2. Mechanical test and material**

The material, which is developed by SNECMA (SAFRAN Group) and considered in this study, is a layer-to-layer interlock woven composite for which a unit cell is shown in Figure 1. The dimensions of the geometrical Representative Volume Element are  $1.8h \times 2h \times h$ . It is made of carbon fibers and epoxy matrix. The weaving is specifically designed for 3D structures to reach stringent specifications under a variety of loading conditions representative of in-service and extreme conditions. To meet these severe requirements and due to the variation of the geometry, more specifically in the blade root, the weaving (*i.e.*, thickness and orientation of the tows) depends on the position within the part. Therefore up to the largest scale, the blade root displays specific heterogeneities or modulations of the local material properties [16].

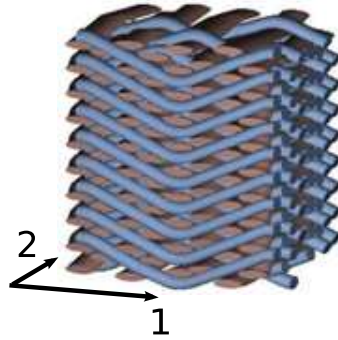


Figure 1: Example of non compacted unit cell made of interlock woven composite used for the test. The warp tows, respectively the weft tows, are along direction 1, respectively direction 2. The dimensions of the geometrical Representative Volume Element, once compacted, are  $1.8h \times 2h \times h$

The studied test consists of pulling a blade root. The sample is put in a dovetail-shaped fixture such that the warp tows are in the observed plane  $Oxz$  and the weft tows are oriented along the normal to this plane. The load is applied on the top part of the sample by a hydraulic jack (Figure 2). Because of this set up, the displacement field is extremely heterogeneous, thereby providing rich data that will be used for identification purposes. However, it is also very complex, namely, the boundary conditions are not well known due to contact and friction on the supporting fixture and the imperfect positioning of the sample. Therefore the present test is instrumented with special care:

- First, acoustic emission is used with two sensors positioned close to the top of the sample to ensure that there is no major damage of the sample during the test.
- The test is also prepared for DIC analyses (Figure 2). A single camera (definition:  $1157 \times 1737$  pixels, digitization: 10 bits) is used for acquiring images during the test to measure the displacement field at each step (see Section 4.1).
- Last, two displacement transducers are positioned on the front surface of the sample to measure possible out-of-plane motions due to sample / actuator misalignments. It would have been possible to correct for them when needed as uncontrolled out-of-plane motions often induce artifacts in the measured in-plane displacement field [17]. However, the levels measured by these transducers were small enough to neglect the effect of out-of-plane motions.

The loading history consists first of the application of a tensile force of half the maximum load level followed, after unloading, by a second force ramp up to the maximum level (Figure 3). The test is load-controlled with a rate of  $F_{\max}/50 \text{ s}^{-1}$  so that the loading conditions are quasi-static. During the whole test, images have been acquired every five seconds. Consequently, 158 images are available.

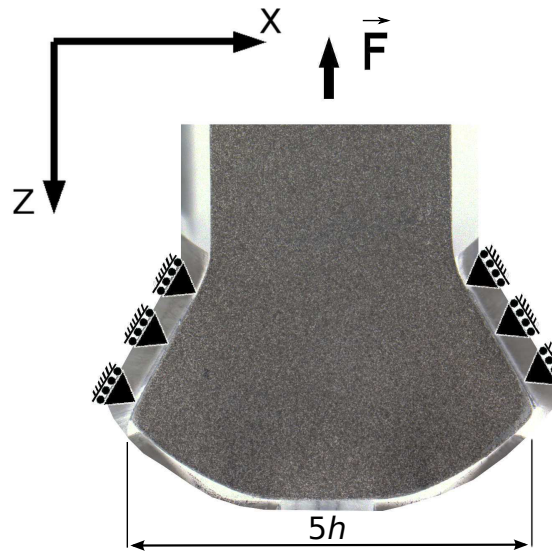


Figure 2: Schematic view of the studied test where the vector  $\vec{F}$  is the applied tensile force when the observed surface has been prepared for correlation purposes

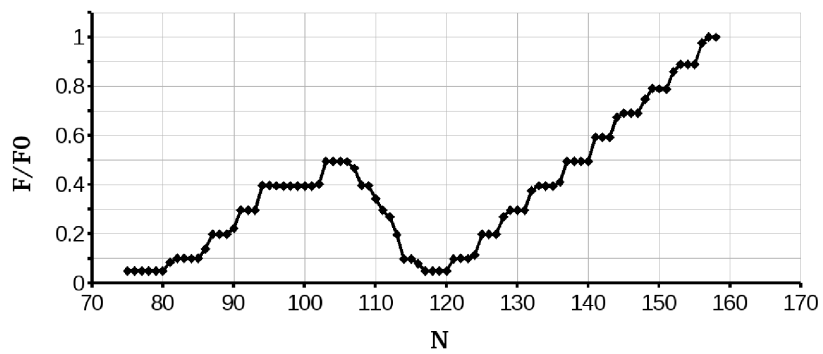


Figure 3: Dimensionless force versus image number

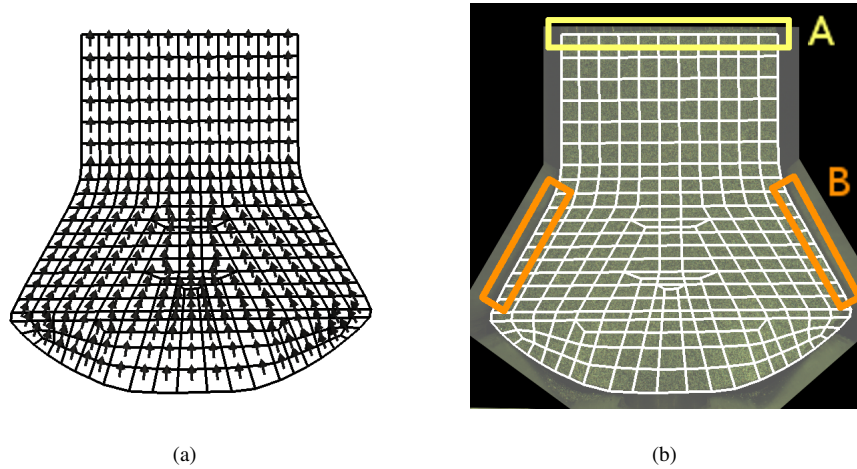


Figure 4: (a) Local orientations of the orthotropy basis are represented as black arrows on the FE mesh used for the simulation. (b) Nodes on which Dirichlet boundary conditions are applied . A: top nodes ('applied load'), B: nodes located at the sample / fixture interface

### 3. Finite Element Model

To compare experimental data with numerical simulations, a finite element model is considered. The latter consists of a two dimensional mesh with quadrilateral elements obtained from the complete three dimensional mesh that was used for design purposes. This mesh of the perfect geometry is 'fitted' to the actual geometry as explained in Section 4.3.2. The sample thickness of  $5h$ , compared to the other two dimensions justifies the two dimensional simplification so that a plane strain hypothesis is a reasonable choice. Based on the classical modeling of composites as an orthotropic elastic medium prior to damage [18, 19], in the material frame given by weft and warp directions, a continuum approach is proposed with spatially varying orthotropy axis orientations. However, in the present study the *same* local elastic behavior is assumed (*i.e.*, that in the material frame). This hypothesis of an orthotropic behavior of the composite is assumed to hold through the entire elastic regime at every point of the solid. With the observed surface, 3D material parameters are the elastic moduli in the weft direction,  $E_1$ , and in the out-of-plane direction,  $E_3$ , the shear modulus,  $G_{13}$ , and Poisson's ratio  $\nu_{13}$ . Local orientations are shown in Figure 4a.

To be consistent with the performed test, the boundary conditions chosen in the simulations are extracted from displacement measurements as Dirichlet conditions prescribed on nodes located on the top side (zone A in Figure 4b) and on the contact surface with the fixture (zone B in Figure 4b). Consequently, there is no need to model the complex interface between the sample and the dovetailed fixture. Elsewhere, a free-edge condition is assumed in accordance with the test. In the following, the study is conducted for a series of images taken during the two macroscopic elastic loadings. The reference image for each of the loading step is taken at the beginning of the ramp, corresponding to a load level equal to 10% of the maximum value.

## 4. Measurement and Identification Tools

### 4.1. Global Digital Image Correlation

Based on images taken during the test, full-field measurements are performed using a global formulation of DIC. In the following, principles of *global* DIC are summarized (more details can be found in Ref. [20]). Section 5 will be devoted to the use of the estimated displacement fields from DIC for identification purposes and uncertainty analyses.

DIC consists of registering two images, one in the reference configuration  $f(\mathbf{x})$ , and another one in the deformed configuration  $g(\mathbf{x})$ , where  $f$  and  $g$  give the gray level value at pixel  $\mathbf{x}$ . It is assumed [21] that the gray level is conserved, up to the camera sensor noise,  $\eta(\mathbf{x})$ , so that

$$g(\mathbf{x} + \mathbf{u}(\mathbf{x})) = f(\mathbf{x}) + \eta(\mathbf{x}) \quad (1)$$

where  $\mathbf{u}$  is the sought displacement field, and  $\eta$  characterizes the acquisition noise. The unknown displacement field is obtained from the minimization of the squared difference  $[g(\mathbf{x} + \mathbf{u}(\mathbf{x})) - f(\mathbf{x})]^2$  summed over all the pixels belonging to the Region Of Interest (ROI)  $\Omega$ . The displacement field  $\mathbf{u}$  is decomposed over a basis of fields whose amplitude is to be determined by minimizing the sum of squared differences. The specificity of *global* DIC lies in the unrestricted choice of this basis of displacement fields. In particular, as will be the case in the present study, a continuous Galerkin basis supported by structured [20] or unstructured [36] meshes can be used. The unknowns of the problem thus become the nodal values of the displacement field,  $u_{\alpha i}$ , and the functional to be minimized is written as

$$\mathcal{T}(u_{\alpha i}) = \int_{\Omega} \left[ g \left( \mathbf{x} + \sum_{\alpha=1}^2 \sum_{i=1}^n u_{\alpha i} N_i(\mathbf{x}) \mathbf{e}_{\alpha} \right) - f(\mathbf{x}) \right]^2 d\mathbf{x} \quad (2)$$

where  $N_i$  is the finite element shape function relative to node  $i$ , and  $\mathbf{e}_{\alpha}$  the unit vector along the  $\alpha$  direction. The functional  $\mathcal{T}$  is minimized iteratively by successive corrections of the deformed image  $g^{(n)}$ , such that  $g^{(n)}(\mathbf{x}) = g(\mathbf{x} + \mathbf{u}^{(n)}(\mathbf{x})) \approx f(\mathbf{x})$  where  $\mathbf{u}^{(n)}$  is the displacement field determined at step  $n$  until  $g^{(n)}$  matches  $f$  (in the sense of a minimum L2-norm of their difference). Incremental corrections of the displacement field  $\delta \mathbf{u}^{(n+1)}$  are computed from the minimization of the linearized form of the objective functional,  $\mathcal{T}_{lin}$

$$\mathcal{T}_{lin}(\delta \mathbf{u}^{(n+1)}) = \int_{\Omega} \left[ g^{(n)}(\mathbf{x}) - f(\mathbf{x}) - \delta \mathbf{u}^{(n+1)} \cdot \nabla f(\mathbf{x}) \right]^2 d\mathbf{x} \quad (3)$$

Corrections to the displacement field  $\delta \mathbf{u}^{(n+1)} = \mathbf{u}^{(n+1)} - \mathbf{u}^{(n)}$  are obtained from this linear form but the convergence is established based on the full (nonlinear) functional  $\mathcal{T}$ . Increments to the nodal displacements  $\delta u_{\alpha i}$ , which are gathered in vector  $\{\delta \mathbf{u}_m\}$ , are obtained from the solution to the following linear system

$$[\mathbf{M}] \{\delta \mathbf{u}_m^{(n+1)}\} = \{\mathbf{b}^{(n)}\} \quad (4)$$

where  $[\mathbf{M}]$  is the global DIC matrix whose components read

$$M_{\alpha i, \beta j} = \int_{\Omega} \partial_{\alpha} f(\mathbf{x}) N_i(\mathbf{x}) \partial_{\beta} f(\mathbf{x}) N_j(\mathbf{x}) \, d\mathbf{x} \quad (5)$$

and  $\{\mathbf{b}^{(n)}\}$  the global DIC vector at iteration  $n$

$$b_{\alpha i}^{(n)} = \int_{\Omega} [g^{(n)}(\mathbf{x}) - f(\mathbf{x})] \partial_{\alpha} f(\mathbf{x}) N_i(\mathbf{x}) \, d\mathbf{x} \quad (6)$$

Note that matrix  $[\mathbf{M}]$  is the same at all iteration steps so that only  $\{\mathbf{b}\}$  has to be updated.

Last, assuming classical speckle patterns such as shown in Figure 2, the modified Newton scheme to solve the minimization problem may lead to trappings in secondary minima of the nonlinear functional  $\mathcal{T}$  for large displacements. To find the global minimum, the first determination of the displacement field is performed on strongly low-pass filtered images, so that large displacements with a coarse description are captured. Based on this first determination, finer and finer details are re-introduced in the images to progressively obtain a more accurate determination of the displacements. This procedure is carried out down to unfiltered images in the final pass. The convergence criterion is based on the infinity norm of  $\delta \mathbf{u}_m^{(n)}$  displacement increment between two consecutive steps and is taken as  $\|\delta \mathbf{u}_m^{(n)}\|_{\infty} < 10^{-3}$  pixel under which the increment on the displacement is of order of the uncertainty. The quality of the measured displacement field is then assessed thanks to the residual map, consisting of the difference  $|f(\mathbf{x}) - g(\mathbf{x} + \mathbf{u}(\mathbf{x}))|$  for every pixel  $\mathbf{x}$  in the domain  $\Omega$ .

Several variants of the implementation of the *global DIC* algorithm have been used in the present study:

- First, the choice is made to account for the gray level correction, by relaxing its conservation (Equation (1)). More precisely, the “corrected-deformed” image,  $g^{(n)}$  is not only advected by the displacement field, but its gray level is rescaled by a quantity  $(1 + c(\mathbf{x}))$  where  $c$  is also decomposed over the same finite-element mesh and shape functions, and the minimization is performed over  $\mathbf{u}$  and  $c$  fields together. Although this procedure increases the number of degrees of freedom, it also corrects the contrast changes between images.
- Second, the gray level interpolation of images can be bilinear, cubic or quintic spline. According to the literature [22, 23], one of the best solutions, which is chosen herein, is computed with B-spline interpolation of gray levels.
- Third, based on this sub-pixel interpolation scheme, evaluations of local gradients and integrations of functional  $\mathcal{T}$  can be performed with a discretization that may differ from the pixel representation of the images. It was chosen to use a summation over the ROI based on midpoints between pixel centers, and to estimate gradients based on centered finite differences at the same midpoints and at the pixel centers.

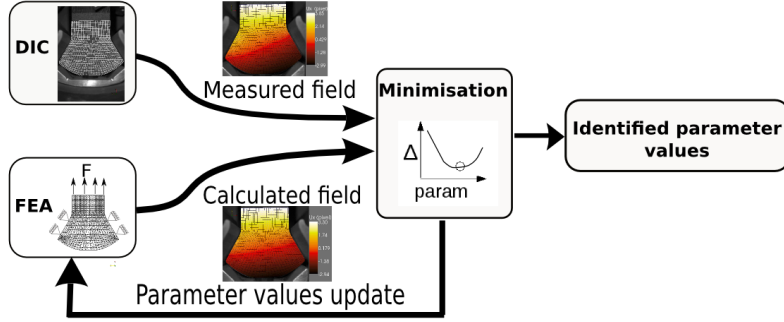


Figure 5: Principle of FEMU where DIC and Finite Element Analyses (FEA) are compared

#### 4.2. Finite Element Model Updating

With the developments of full-field measurement techniques, several identification procedures to evaluate material parameters from these fields have been developed [24]. Finite Element Model Updating [25] (FEMU) is the most generic and intuitive method. It can be based on over-determined data, a full-field displacement measurement in the present case, and allows complex geometries and / or constitutive laws to be studied. The principle consists of finding iteratively parameter values introduced in Finite Element (FE) simulations to minimize the cost function,  $\mathcal{R}$ , assessing the gap between measured nodal displacements, say by DIC,  $\{\mathbf{u}_m\}$ , and computed ones  $\{\mathbf{u}_c\}$  (Figure 5)

$$\mathcal{R}^2 = (\{\mathbf{u}_m\} - \{\mathbf{u}_c\})^t [\mathbf{C}_u]^{-1} (\{\mathbf{u}_m\} - \{\mathbf{u}_c\}) \quad (7)$$

It is worth emphasizing that the cost function, Equation (7), is based on the displacement field itself, in contrast with most classical approaches that rely on strain fields [24, 26]. This choice is made to reduce the sensitivity to high frequency noise modes present in the displacement field due to the measurement technique itself, and amplified by the derivation of this field needed to obtain the strain field (the alternative being to smooth out the strain field based on arbitrary *a priori* assumptions). In Equation (7),  $[\mathbf{C}_u]$  is the covariance matrix of the nodal displacements measured by DIC (*i.e.*,  $\mathcal{R}^2$  is proportional to the chi-squared error). When noise is the dominant source of variability,  $[\mathbf{C}]$  can be evaluated exactly as proportional to matrix  $[\mathbf{M}]^{-1}$  [20, 27]. It provides a weighting of the kinematic degrees of freedom based on the measurement and the texture of the analyzed pictures.

The minimization of  $\mathcal{R}$  is performed with a Newton-Raphson algorithm updating the set of unknown parameters  $\{\mathbf{p}\}$  at each iteration. Let  $\{\mathbf{p}^0\}$  denote their initial value, and  $\{\mathbf{p}^{(s)}\}$  that of iteration  $s$ . The increment  $\{\delta\mathbf{p}^{(s+1)}\}$  is equal to  $\{\mathbf{p}^{(s+1)}\} - \{\mathbf{p}^{(s)}\}$ . The latter is shown to obey

$$\{\delta\mathbf{p}^{(s+1)}\} = ([\mathbf{P}^{(s)}]^t [\mathbf{M}] [\mathbf{P}^{(s)}])^{-1} [\mathbf{P}^{(s)}]^t [\mathbf{M}] (\{\mathbf{u}_m\} - \{\mathbf{u}_c^{(s)}\}) \quad (8)$$

with

$$P_{ij}^{(s)} = \frac{\partial (u_c^{(s)})_i}{\partial p_j^{(s)}} \quad (9)$$

where  $[\mathbf{P}^{(s)}]$  is the sensitivity of the computed displacement field  $\mathbf{u}_c^{(s)}$  with respect to the sought parameters  $\{\mathbf{p}^{(s)}\}$  at iteration  $s$ .

### 4.3. Numerical Implementation

#### 4.3.1. Specific Environment

As described previously, the FEMU method relies on the comparison of displacement fields obtained by measurement, and taken as reference, and those obtained by an FEA. It is essential to superimpose the calculated displacement field onto the measured one [28]. Usually, simulations and measurements are carried out with different softwares. Consequently, reference points that will be positioned in the simulation are considered but this introduces additional interpolation errors and uncertainties. The dialog between simulation and experimental data can also be limited by the common assumption that the loading conditions of the simulation are ideal boundary conditions that are not reflecting the inherent imperfection of the test. However, actual boundary conditions can be extracted from DIC measurements and (typically scarce) static loading information (*e.g.* resultant force or torque) measured by different sensors.

The recourse to DIC measured displacements as boundary conditions emphasizes the necessity to adjust precisely the mesh onto the actual geometry as captured in images. Furthermore, the errors and uncertainties due to projection and interpolation, when the measured displacement field is compared to the simulated one, are avoided by working on the very same mesh for the measurement and the simulation. The measured displacement field is obtained at the same points as the simulated displacement field. This is easier if a unique environment is utilized for global DIC and mechanical modeling as both of these tasks have been formalized in the same framework. Thus a specific C++ environment, called “Metil” [29, 30], has been designed in-house to efficiently manage the required *seamless* exchange of information between DIC and FEMU procedures.

#### 4.3.2. Mesh Import

A first mesh has been designed with the commercial FE code ABAQUS™. It is imported in the C++ environment and to adjust it onto the reference on which the DIC analysis is based. The geometry, the different material properties and the local orientation of the orthotropy axes (Figure 4a) are also imported by reading the input file generated by ABAQUS™. Then, the mesh has to be adjusted and scaled onto the image since the references (and length units) are different. The proposed adjustment is again based on DIC between two binary masks, namely, one created on the reference picture and a second on the FE mesh. A global DIC is performed authorizing only rigid body motions and

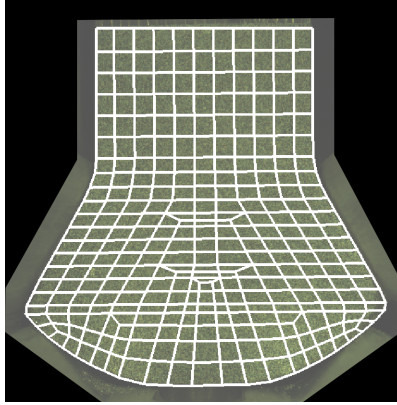


Figure 6: Finite-Element mesh fitted onto the reference picture using DIC with rigid-body motions and a pure dilatational field

a uniform dilation. By applying the obtained displacement field to the FE mesh, the latter is adjusted onto the image (Figure 6).

This procedure takes into account the real geometry of the sample and seeks for the best adjustment of the perfect mesh on the real sample geometry. However, slight differences between the perfect geometry and real boundaries may exist. These can be due to fabrication tolerances. Consequently, the considered mesh can be corrected to benefit from the knowledge of the *actual geometry* of the sample. A projection of the boundary nodes of the FE mesh onto the known boundary of the real geometry is finally performed [31].

## 5. Identification and Uncertainty Analysis

### 5.1. Identification Results

As explained in Section 3, only kinematic data or free edge conditions are used as boundary conditions. They are extracted from the measured displacement field shown in Figure 7 for the pair of images 123 – 139, corresponding to 50% of the maximum load level. Since the macroscopic loading corresponds to an elastic step, the dynamic range of the displacement fields along the two in-plane directions is low and is about four pixels.

The identification of elastic parameters will be performed in two steps. First, the elastic modulus  $E_1$  is fixed to its nominal value, and the three other material parameters are identified as the ratios  $\ln(G_{13}/E_1)$  and  $\ln(E_3/E_1)$  and Poisson's ratio  $\nu_{13}$ . Second, the elastic modulus is set so that the sum of nodal forces of nodes A (Figure 4b) matches the measured resultant force. The elastic parameters are ordered as  $\{\mathbf{p}\}^t = \{\ln(G_{13}/E_1), \ln(E_3/E_1), \nu_{13}\}$ . The chosen parameters are the logarithms of the elastic moduli so that the elastic constants always remain positive. Specific limits are imposed by breaking the iterative procedure if the Poisson's ratios do not satisfy the positivity of the elastic energy (*i.e.*,  $1 - \nu_{13}\nu_{31} > 0$ ).

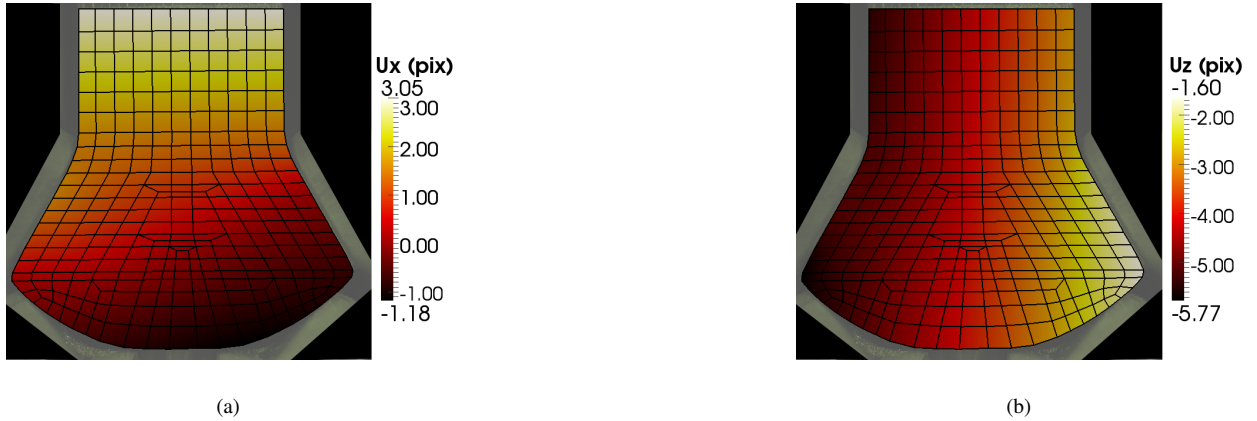


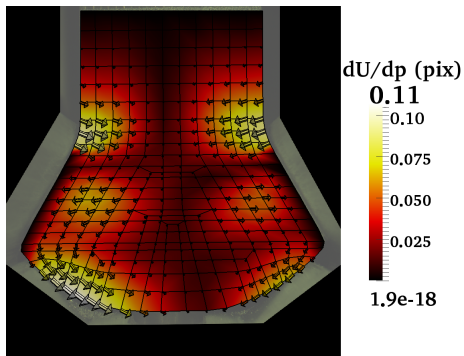
Figure 7: Measured displacement fields  $\mathbf{u}_m$  projected onto (a) the  $x$ -axis and (b) the  $z$ -axis. Units are given in pixel

In the implemented FEMU technique, a Newton-Raphson algorithm is used to perform the minimization, and hence the sensitivity of the displacement field has to be characterized with respect to each sought parameter. The relative sensitivity maps are obtained from an FEA using a symbolic calculus approach as far as possible in the computation to ensure good accuracy. The material properties are initially set to values close to the nominal ones. For the three material parameters, the relative sensitivity maps are shown in Figure 8. The location of sensitive parts is mainly on the lower part of the blade root, corresponding to large variations in the displacement field. Equation (8) is relaxed such that if one of the calculated increment  $\delta p_i$  is greater than 10% of the nominal value of the corresponding parameter  $p_i$ , then the effective increment at iteration  $s$  is  $0.1\{\delta \mathbf{p}^{(s)}\}$ . By solving iteratively Equation (8), fast convergence to the solution that minimizes the residual,  $\mathcal{R}$ , is observed. This procedure is led for the pair of images corresponding to half the maximum load. The results of the first step, shown in Figure 9, indicate that the iterative scheme converges. However, the identified Poisson's ratio  $\nu_{13}$  is far from the nominal value. The break observed around iteration 80 corresponds to the transition from relaxed increments to total ones.

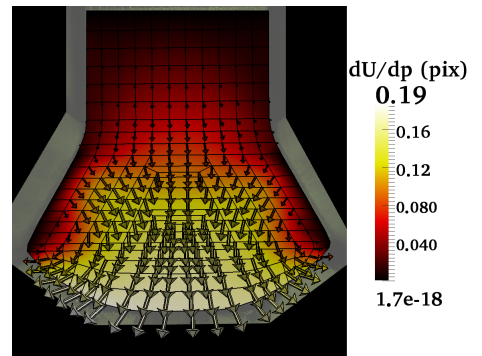
In the following section, the effect of noise on the identification of material parameters will be discussed.

## 5.2. Uncertainty Analysis

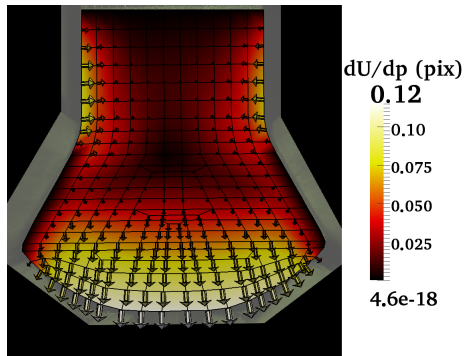
The quantification of the uncertainty of each identified parameter based on the identification method is now addressed. The sensitivity maps are indicative of the expected uncertainty on each identified parameter due to the presence of noise in images. *Global DIC*, coupled with FEMU, is perfectly suited to trace these uncertainties. The covariance matrix of the displacement field measured by DIC, when noise is the dominant source of variability, is proportional to the inverse of the global DIC matrix  $[\mathbf{M}]$  [27, 32, 33]. In the following, let us focus on the uncertainties obtained at convergence of the identification algorithm. Consequently, the sensitivity matrix  $[\mathbf{P}]$  (see Equation (9)) is



(a)

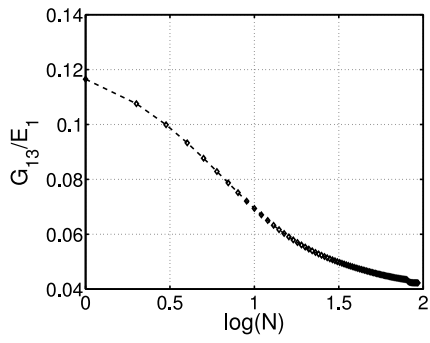


(b)

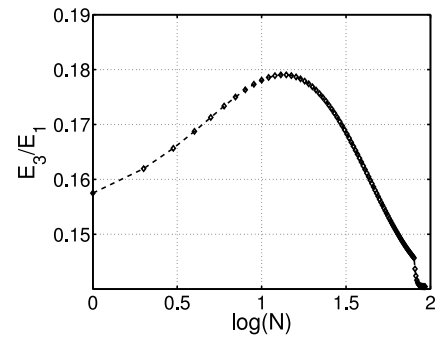


(c)

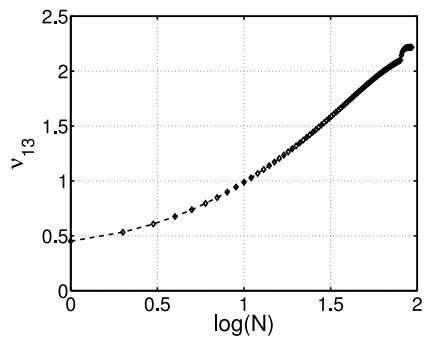
Figure 8: Norm of the relative sensitivity maps for the three material parameters, (a)  $\ln(G_{13}/E_1)$ , (b)  $\ln(E_3/E_1)$  and (c)  $\nu_{13}$ , which are shown with nodal vectors amplified 500 times



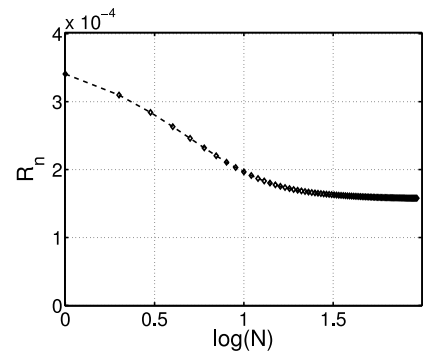
(a)



(b)



(c)



(d)

Figure 9: Change of the three identified material parameters, (a)  $G_{13}/E_1$ , (b)  $E_3/E_1$  and (c)  $\nu_{13}$ , and (d) the normalized residual  $R_n = \frac{(\{\mathbf{u}_m\} - \{\mathbf{u}_c\})[\mathbf{M}](\{\mathbf{u}_m - \mathbf{u}_c\})}{\{\mathbf{u}_m\}[\mathbf{M}]\{\mathbf{u}_m\}}$  with base 10 logarithm of the iteration number  $N$

computed for this last step. Let  $\{\delta\mathbf{u}\}$  and  $\{\delta\mathbf{p}\}$  denote the deviations from the converged value of the displacement field and material parameters due to noise. They are related by an expression similar to Equation (8)

$$\{\delta\mathbf{p}\} = ([\mathbf{P}]^t[\mathbf{M}][\mathbf{P}])^{-1}[\mathbf{P}]^t[\mathbf{M}]\{\delta\mathbf{u}\} \quad (10)$$

Defining  $\sigma^2$  as the variance of image noise (assumed to be Gaussian and uncorrelated at the pixel scale), the covariance matrix of the identified parameters is readily obtained [20]

$$[\mathbf{C}_u] \equiv \langle \{\delta\mathbf{u}\} \otimes \{\delta\mathbf{u}\} \rangle = 2\sigma^2[\mathbf{M}]^{-1} \quad (11)$$

where  $\langle \bullet \rangle$  denotes the ensemble average, and Equation (10) leads to

$$[\mathbf{C}_p] \equiv \langle \delta\mathbf{p} \otimes \delta\mathbf{p} \rangle = 2\sigma^2([\mathbf{P}]^t[\mathbf{M}][\mathbf{P}])^{-1} \quad (12)$$

where the diagonal terms give the variance for each parameter separately, all the others being fixed to their nominal value, but the covariance matrix allows the entire uncertainty to be further analyzed by taking into account all couplings between parameters.

The eigenvalues of matrix  $[\mathbf{N}] \equiv [\mathbf{P}]^t[\mathbf{M}][\mathbf{P}]$  give access to the modes that can be determined by the mechanical test sorted according to their uncertainty. We will come back later on to this crucial point and propose a regularization strategy to get a more operative method for identification purposes. Let us introduce the matrix  $[\mathbf{V}]$  of eigenvectors, and  $[\mathbf{D}]$  the diagonal matrix of eigenvalues, so that

$$[\mathbf{N}] = [\mathbf{V}]^t[\mathbf{D}][\mathbf{V}] \quad (13)$$

The variance of the determined amplitude of the  $i$ -th eigenvector reads

$$\tau_i^2 = \frac{2\sigma^2}{D_{ii}} \quad (14)$$

and that of parameter  $p_k$

$$\sigma_{p_k}^2 = 2\sigma^2 \sum_i \frac{V_{ki}^2}{D_{ii}} \quad (15)$$

Note that the latter equation takes into account the fluctuations of all parameters, and does not assume that they are fixed in contrast with just selecting the diagonal element of  $[\mathbf{N}]$ .

It is to be stressed that the above uncertainties are only those related to image noise coming from the CCD camera, but other factors may also affect the identification quality (such as an erroneous model framework, microstructure effects or imperfections in the test that are not taken into account in the model).

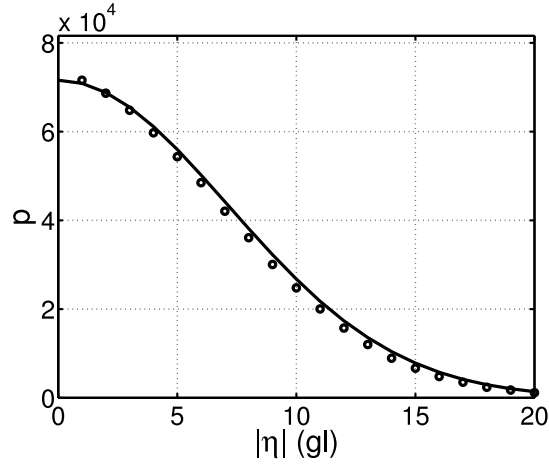
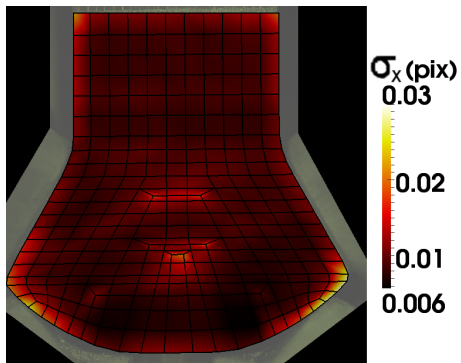


Figure 10: Histogram obtained from the pixel-to-pixel absolute difference between images. Data points are shown as open circles, and Gaussian fit (solid curve) is shown as a guide to the eye. The dynamic range of the reference picture is 1024 gray levels

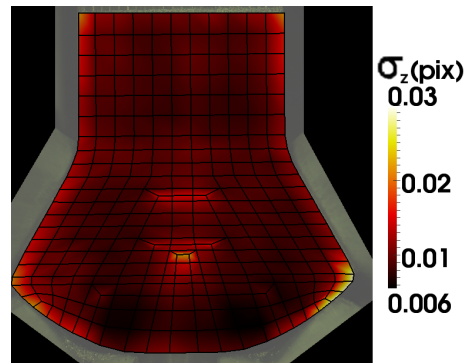
### 5.3. Application

The sensor noise, which is characterized by its standard deviation  $\sigma$ , is identified from several images taken at the same unloaded state. Each image is encoded over 10-bit deep gray levels (*i.e.*, ranging from 0 to 1023). The statistical distribution of gray level fluctuations for all the pixels is shown in Figure 10. It is observed that a Gaussian fit gives a very good account of these fluctuations. A standard deviation of  $\sigma = 5.5$  gray levels is obtained. Based on this characterization of camera noise, the displacement uncertainty on each mesh node is computed with Equation (11) and shown for the studied blade root mesh (Figure 11a-b). For the sake of simplicity, only the diagonal of matrix  $[\mathbf{M}^{-1}]$  is considered. It is worth noting that the latter is a band matrix so that non diagonal terms, which contribute to uncertainty, are not predominant. This theoretical result is compared with uncertainties obtained from 72 DIC calculations performed between image pairs taken for a load free specimen. The standard deviation of the displacement obtained for each node is also shown on the mesh (Figure 11c-d). The maps show that the displacement determination is more affected by noise on the boundary because external nodes are less constrained than inner ones [34]. Furthermore, the surface area of the element is also an influential factor so that the central small elements have a high uncertainty as compared with larger elements. The poor accuracy observed on the bottom part of the mesh is due to the poor gray level texture of the surface. The similarity of both maps for each displacement component validates the use of matrix  $[\mathbf{M}]$  computed for DIC to model the displacement uncertainty resulting from the camera noise. This validation is important inasmuch as the covariance matrix provides the weighting used in Equation (7).

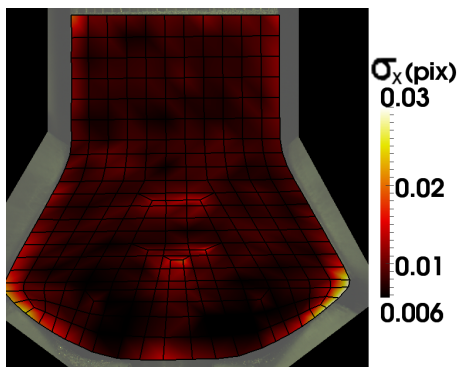
The quality of the identification can also be estimated in terms of gray level residuals to be compared with the



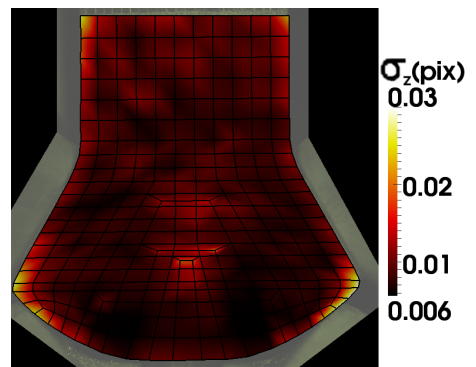
(a)



(b)



(c)



(d)

Figure 11: Uncertainty maps calculated on mesh nodes from matrix  $[M]$  used in DIC and the CCD sensor noise, (a) along the  $x$ -axis, and (b)  $z$ -axis, and obtained from several DIC calculations on image pairs, (c) along the  $x$ -axis, and (d)  $z$ -axis

previous results. For any displacement field  $\mathbf{u}$ , the picture in the deformed configuration  $g$  can be corrected to  $g(\mathbf{x} + \mathbf{u}_m(\mathbf{x}))$ , where  $\mathbf{u}_m$  denotes the measured displacement field. The gray level residual is defined as  $\rho_m(\mathbf{x}) = |g(\mathbf{x} + \mathbf{u}_m(\mathbf{x})) - f(\mathbf{x})|$ . It would reduce to image noise (*i.e.*,  $\eta$ , see Equation (1)) if the chosen displacement basis were consistent with the actual kinematics. Figure 12a shows the map of  $\rho_m$ . Except for few points its level remains very low. Its standard deviation  $\sigma_m = 6.8$  gray levels is very close to that of pure noise (*i.e.*,  $\sigma = 5.5$  gray levels). This result validates the use of the measured displacement field for identification purposes.

Similarly, the displacement field  $\mathbf{u}_c$  computed with the identified material parameters can be used to evaluate a gray level residual  $\rho_c(\mathbf{x}) = |g(\mathbf{x} + \mathbf{u}_c(\mathbf{x})) - f(\mathbf{x})|$ . The latter will quantify the quality of the identification and its distance to the gray level residuals induced by acquisition noise. Figure 12b shows the corresponding map, which is very close to that of  $\rho_m$ . The corresponding standard deviation  $\sigma_c = 8.2$  gray levels is again close to that of pure noise (*i.e.*,  $\sigma = 5.5$  gray levels). This result validates the identification result. Last, to measure the distance between the measured and computed displacement fields, the difference of the two previous residuals is considered. There are fewer discrepancies than in the two previous maps (Figure 12c). All these results are summarized by plotting the histograms of Figure 12d. A slight increase is observed between the gray level residuals associated with noise alone, the measured and calculated displacement fields. However, when the difference between the measured and calculated displacement fields is analyzed, it clearly leads to lower levels.

The evaluation of the uncertainty is now considered based on Equation (12). Let us recall that the elastic parameters have been chosen as  $\{\mathbf{p}\}^t = \{\ln(G_{13}/E_1), \ln(E_3/E_1), \nu_{13}\}$ . Matrix  $[\mathbf{N}] = [\mathbf{P}]^t[\mathbf{M}][\mathbf{P}]$  is computed to be

$$[\mathbf{N}] = 10^6 \times \begin{pmatrix} 2.4 & 3.3 & 1.9 \\ 3.3 & 93.6 & 33.5 \\ 1.9 & 33.5 & 14.6 \end{pmatrix} \quad (16)$$

The resulting uncertainty from Equation (12) for each of the parameters considering the other ones to be known is simply read from the diagonal elements of  $[\mathbf{C}_p]$ , as listed in Table 1. To get a better understanding of the standard uncertainty, it is convenient to diagonalize matrix  $[\mathbf{N}]$ . The eigenvectors are the columns of matrix  $[\mathbf{V}]$

$$[\mathbf{V}] = \begin{pmatrix} 0.71 & 0.21 & -0.66 \\ 0.69 & -0.27 & 0.66 \\ -0.04 & -0.94 & -0.34 \end{pmatrix} \quad (17)$$

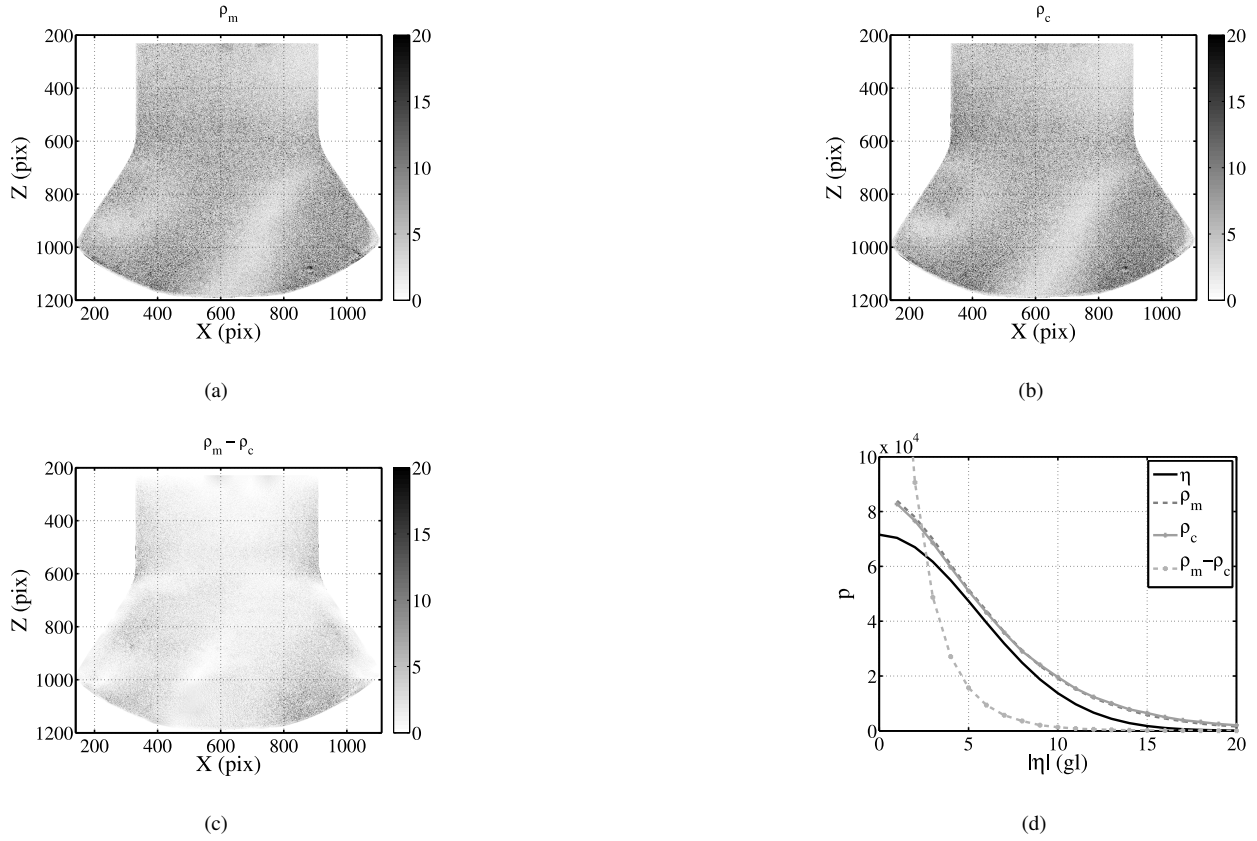
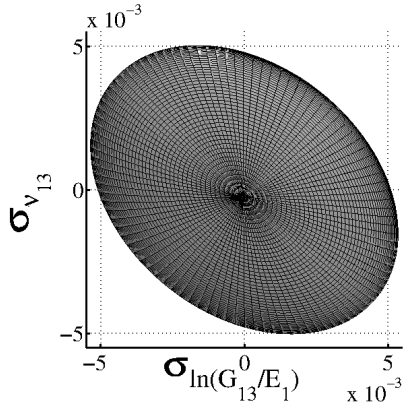


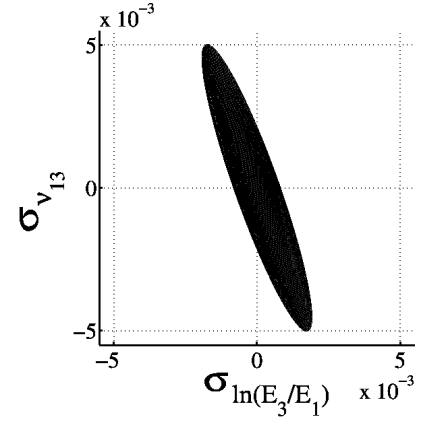
Figure 12: Gray level residuals associated with a measurement and an identification step: (a) measurement residual  $\rho_m$ , (b) identification residual  $\rho_c$ , (c)  $\rho_m - \rho_c$ . (d) Histograms of gray levels of  $\eta$ ,  $\rho_m$ ,  $\rho_c$ ,  $\rho_m - \rho_c$ . The dynamic range of the reference picture is 1024 gray levels

Table 1: Standard uncertainty of each identified parameter considering the other ones as fixed (column 2) or taking into account the full variability of each parameter (column 3)

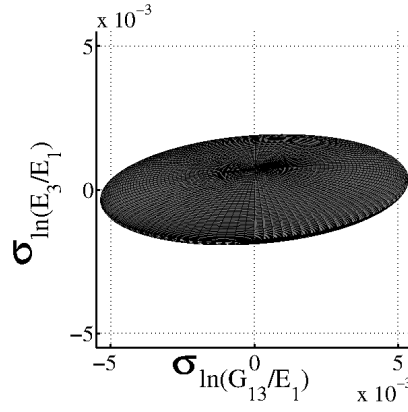
Parameter	Identified value	Single parameter uncertainty	Full uncertainty
$\ln(G_{13}/E_1)$	$\ln(0.042)$	$5 \times 10^{-3}$	$5.3 \times 10^{-3}$
$\ln(E_3/E_1)$	$\ln(0.14)$	$0.8 \times 10^{-3}$	$1.9 \times 10^{-3}$
$\nu_{13}$	2.2	$2 \times 10^{-3}$	$5 \times 10^{-3}$



(a)



(b)



(c)

Figure 13: Uncertainty projection in the three planes (a)  $(\nu_{13}, \ln(G_{13}/E_1))$ , (b)  $(\nu_{13}, \ln(E_3/E_1))$  and (c)  $(\ln(E_3/E_1), \ln(G_{13}/E_1))$

and the corresponding eigenvalues are

$$[\mathbf{D}] = 10^6 \times \begin{pmatrix} 1.6 & 0 & 0 \\ 0 & 3.0 & 0 \\ 0 & 0 & 106.1 \end{pmatrix} \quad (18)$$

The first two eigenvectors of minimum eigenvalue are a combination of the first,  $\ln(G_{13}/E_1)$ , and third,  $\nu_{13}$ , identified parameters. And the third eigenvector is mostly aligned with the second parameter  $\ln(E_3/E_1)$ . This last eigenvector has a much higher eigenvalue, and consequently a lower uncertainty than that of Poisson's ratio and shear modulus. Figure 13 shows the plots of the projection of the uncertainty domain in each plane of two parameters. The full parameter uncertainty can easily be read as the projections of the ellipsoid whereas the single parameter uncertainty corresponds to the intercept with the axis.

The variance of the amplitude of the three eigenmodes is given by

$$\tau^2 = 10^{-6} \times \begin{pmatrix} 37.8 \\ 20.2 \\ 0.6 \end{pmatrix} \quad (19)$$

As derived from Equation (15), the full standard uncertainties on the three parameters are given in Table 1. The noise is mostly affecting the determination of the Poisson's ratio and shear modulus, as the uncertainty reaches its highest value (*i.e.*, 0.005). However, the third parameter displays a low uncertainty with respect to the camera noise. Furthermore, the determination of the Poisson's ratio and shear modulus is coupled as shown by the eigenvectors (Equation (17)).

#### 5.4. Regularization

In cases where some parameters cannot be determined with the available mechanical test, it may lead to the conclusion that no parameter can be safely evaluated (*i.e.*, their full uncertainty may be prohibitively high or as it is the case herein, their coupling with other parameters impedes their evaluation) in spite of the fact that the identification may provide constraints on combinations of parameters. To deal with such a very common situation, it is proposed to introduce a regularization strategy.

Since the experimental data lack the needed information to provide in an autonomous fashion the evaluation of the sought parameters, the only option is to supply the identification procedure with some prior (exogenous) information on the parameters. This is designed to limit the degrees of freedom that are not determined by the experimental test and to leave mostly unaffected the other ones. This additional information is chosen as the proximity of parameters to nominal values  $\{\mathbf{p}^{nom}\}$  (*e.g.* estimated by homogenization results or any other means unrelated to the present experiment). In that case, nominal values are obtained from simple tensile test for in-plane elastic modulus,  $E_1$ , Iosipescu test for shear modulus,  $G_{13}$  and homogenization for Poisson's ratio,  $\nu_{13}$  and out-of-plane elastic modulus,  $E_3$  based on the Eshelby inclusion method [35, 9]. Six tests for each material parameter have been conducted from which the mean value is taken as nominal value and the standard deviation as its uncertainty. The resulting scatter is higher on the shear modulus, 4%, than on in-plane elastic modulus, 2%. However, the uncertainty coming from the homogenization theory is difficult to estimate.

To associate information coming from two different channels, it is proposed to minimize a joint objective functional. The one considered up to this point is written as  $T_1(\{\mathbf{p}\}) = \|\{\mathbf{u}_m\} - \{\mathbf{u}_c(\{\mathbf{p}\})\}\|_M^2$ , where the norm is derived from the metric induced by the covariance matrix of  $\{\mathbf{u}_m\}$  (*i.e.*, chi-squared error). The additional information can simply be written as  $T_2(\{\mathbf{p}\}) = \Psi(\{\mathbf{p}\} - \{\mathbf{p}^{nom}\})$ , where  $\Psi$  is a convex function reaching its minimum

at the origin. The solution to this regularized problem will be the minimum of  $T_{tot} = T_1 + T_2$ . The difficulty is to design a  $\Psi$  function that allows for a fair comparison of information on  $\{\mathbf{p}\}$  coming from different sources. The common “gauge” is provided by the uncertainty. Thus the exogenous information  $\{\mathbf{p}^{nom}\}$  is assumed to be provided together with its uncertainty. The latter ideally should be a full covariance matrix,  $[\mathbf{C}^{nom}]$  but in most practical cases, the nominal values of  $\{\mathbf{p}\}$  will be determined independently from each other so that this covariance matrix is diagonal  $C_{ij}^{nom} = (\sigma_{ii}^{nom})^2 \delta_{ij}$ . Thus it is proposed to choose as  $\Psi$  the norm induced by the inverse covariance metric,

$$T_2(\{\mathbf{p}\}) = A(\{\mathbf{p}\} - \{\mathbf{p}^{nom}\})^t [\mathbf{C}^{nom}]^{-1} (\{\mathbf{p}\} - \{\mathbf{p}^{nom}\}) \quad (20)$$

where  $A$  is a parameter to be determined. Image noise by itself (assuming no other source of bias, or model error) will make the minimum value of  $T_1$  of the order of  $T_1^* = 6.46 \times 10^7$  as previously derived for the image pair 123 – 139. Thus a similar value of  $T_2$  should correspond to the nominal uncertainty on the corresponding parameters. It is chosen to consider a global uncertainty (*i.e.*, variance  $(\sigma^{nom})^2$ ) as the mean of the variance of each parameter. A fair global value of the uncertainty on material parameters can be fixed at 4% (Table 2). Thus  $A/(\sigma^{nom})^2 = \lambda^*$ .

The problem to solve now takes a form similar to the previous Newton-Raphson iteration

$$([\mathbf{N}] + \lambda^*[\mathbf{I}])\{\delta\mathbf{p}\} = [\mathbf{P}]^t[\mathbf{M}](\{\mathbf{u}_m\} - \{\mathbf{u}_c\}) + \lambda^*(\{\mathbf{p}^{nom}\} - \{\mathbf{p}\}) \quad (21)$$

In the present example, it is further assumed that the nominal uncertainty is uniform on the chosen parameters so that  $T_2$  is simply proportional to the Euclidean norm of vector  $(\{\mathbf{p}^{nom}\} - \{\mathbf{p}\})$ . In this case, the interference between both parts of the problem  $T_1$  and  $T_2$  can simply be read according to the spectrum of eigenvalues of  $[\mathbf{N}]$  since in the basis where  $T_1$  is diagonal, so will  $T_2$  be. The  $T_2$  functional provides a threshold for the  $T_1$  eigenvalues, selecting the modes set by the experimental observation, and those mostly dictated by the nominal values.

Minimization of the joint functional  $T_{tot}$  allows for finding a compromise between the two sources of information. However, the interpretation of the value of the resulting solution is a crucial point. It would be inappropriate to repeat the previous analysis of the resulting uncertainty based on the total functional, as it does not do justice to the compatibility between the experimental and nominal information. It is proposed to consider separately  $T_1$  and  $T_2$  for the obtained solution. Each of these two terms will provide a measurement of the likelihood of the corresponding result. Therefore one may find that either the additional information on the nominal values of the parameters is or is not consistent with the experimental observation and identification. An inconsistency may be the sign of an inappropriate modeling (*e.g.* unduly portraying the material as homogeneous) or an erroneous nominal value.

Due to the coupling between the three parameters (Equation (17)), the three identified values have changed. The uncertainties due to acquisition noise are recalled in Table 2 as well as the initial, nominal and identified values. Regarding these uncertainties and the ones on the nominal values, the identified value of the elastic modulus  $E_3$  is

Table 2: Identified values and full standard uncertainty of each parameter determined with the regularized approach

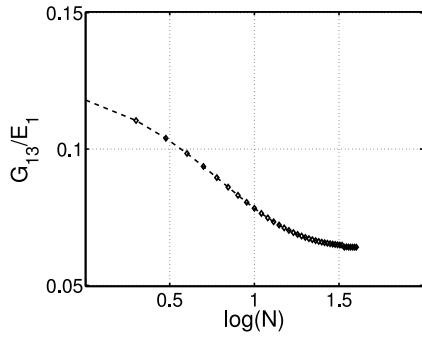
Parameter	Initial value	Nominal value	Identified value	Full uncertainty from sensor noise	Uncertainty on nominal value
$\ln(G_{13}/E_1)$	$\ln(0.127)$	$\ln(0.097)$	$\ln(0.064)$	$5.3 \times 10^{-3}$	$4 \times 10^{-2}$
$\ln(E_3/E_1)$	$\ln(0.153)$	$\ln(0.182)$	$\ln(0.193)$	$1.9 \times 10^{-3}$	$4 \times 10^{-2}$
$\nu_{13}$	0.36	0.46	1.19	$5 \times 10^{-3}$	$4 \times 10^{-2}$

compatible with the nominal value. However, this is not the case for the two other parameters, the shear modulus and Poisson's ratio.

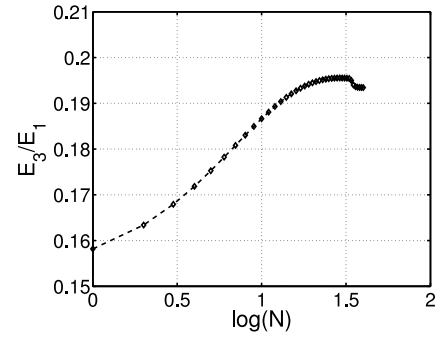
Plots of the parameter change,  $p_i$ , with the iteration number  $N$  are shown in Figure 14. A stationary solution is reached within about 40 iterations. The global residual change (Figure 15) confirms this fast convergence. The elastic modulus  $E_1$  is finally adjusted so that the resulting tensile load obtained from the modeling matches the experimental value.

The difference between measured and computed displacements quantifies the quality of the identification (Figure 16). In the upper part of the mesh where a homogeneous modeling is appropriate for the effective microstructure, local residuals projected onto the  $z$ -axis are low, *i.e.*, one to ten times the displacement uncertainty found in DIC (*i.e.*, 0.01 pixel). However, the local residuals projected onto the  $x$ -axis in the same region are about twenty to forty times higher than the displacement uncertainty. It is to be emphasized that the determination of the material parameters is uniform over the whole FE, and hence a compromise is selected to minimize the difference in displacements over the entire analyzed region. Figure 17a shows the gray level residual  $\rho_m$  for the measured displacement. Similarly, Figure 17b shows the capacity of the updated FE model to match the experiment. The error induced by the identification process is shown by the difference between the two gray level residuals (Figure 17c). These results are again summarized in terms of histograms in Figure 17d. The same trends as those observed in Section 5.3 are observed with the regularized approach.

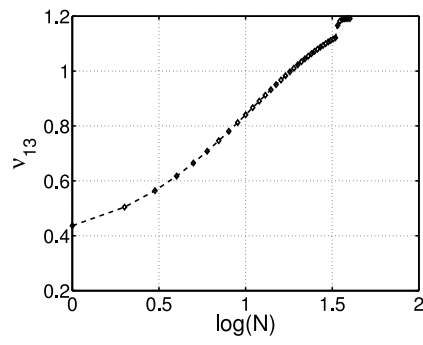
The residual fields (Figures 16 and 17c) signal that the modeling hypothesis (*i.e.*, homogeneous and orthotropic elasticity) is inappropriate to fully account for the measured displacement field in the sense that the residual field does not appear to be comparable to be simply noise. Large scale features in the residual field are a motivation to revisit the modeling framework. Let us stress that in practice the final decision on the appropriate framework is often a compromise between sophistication and simplicity. However, even if the chosen modeling is simpler than what could



(a)



(b)



(c)

Figure 14: Parameter changes: (a)  $G_{13}/E_1$ , (b)  $E_3/E_1$  and (c)  $\nu_{13}$  versus base 10 logarithm of the iteration number  $N$

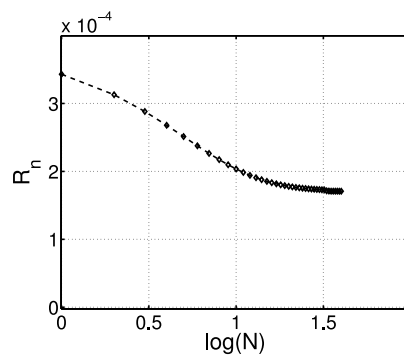


Figure 15: Change of the residual,  $R_n$ , with base 10 logarithm of the iteration number,  $N$

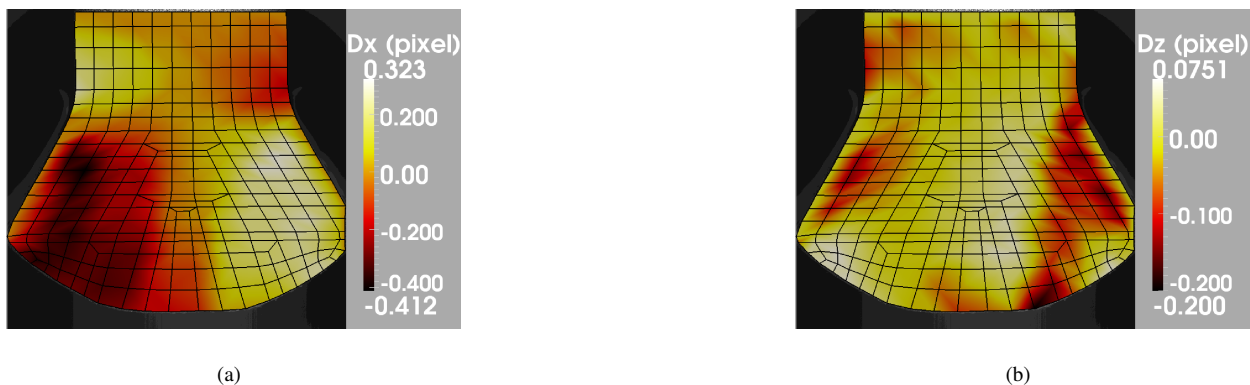


Figure 16: Local displacement residual (*i.e.*, difference  $\mathbf{u}_m - \mathbf{u}_c$ ) projected onto (a) the  $x$ -axis, and (b) the  $z$ -axis. Units are in pixel

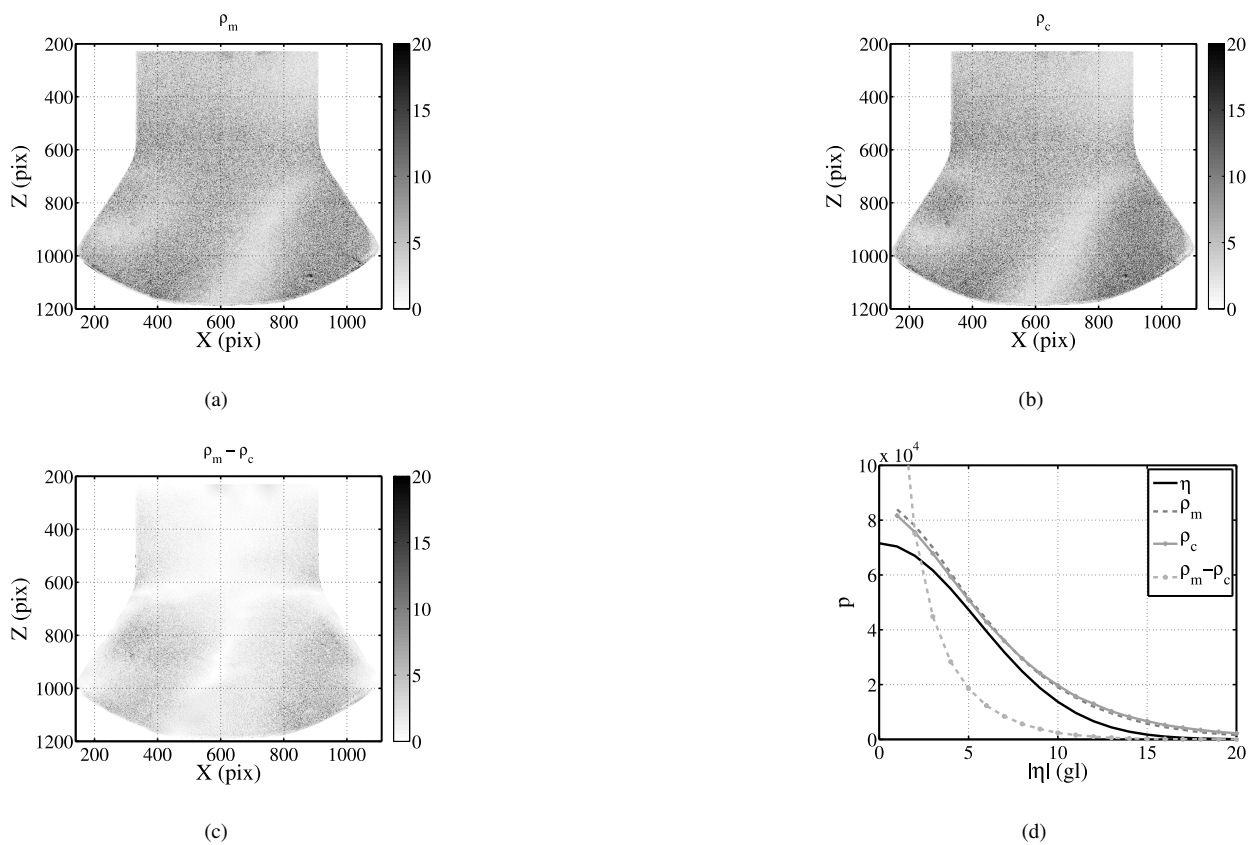


Figure 17: Gray level residuals associated with a measurement and a regularized identification step: (a) measurement residual  $\rho_m$ , (b) identification residual  $\rho_c$ , (c)  $\rho_m - \rho_c$ . (d) Histograms of gray levels of  $\eta$ ,  $\rho_m$ ,  $\rho_c$ ,  $\rho_m - \rho_c$ . The dynamic range of the reference picture is 1024 gray levels

be considered, it is extremely valuable to come up with a tool that provides the most appropriate parameter values. In the present case, it appears likely that a refined description (*e.g.* spatially heterogeneous elastic properties) would allow for a better match between modeling and observation. This point will be addressed in Section 5.5.

Up to now, only a single pair of images was studied. The results obtained for the two loading ramps are shown in Figure 18. The first ramp up to half the maximum load is shown in dark color, and the second one in light gray, and for the original ( $\lambda^* = 0$ ) and regularized ( $\lambda^* \neq 0$ ) identification procedures.

For small load levels without regularization, the material parameters are not well determined and exhibit high fluctuations due to coupling effects and low signal/noise ratios. This is shown by the high uncertainties observed in Figure 19. The global dimensionless residual,  $R_n = (\{\mathbf{u}_m\} - \{\mathbf{u}_c\})[\mathbf{M}](\{\mathbf{u}_m\} - \{\mathbf{u}_c\})/(\{\mathbf{u}_m\}[\mathbf{M}]\{\mathbf{u}_m\})$ , is very high as compared with higher load levels. Thanks to the regularization, these erratic identified values are reasonably stabilized even for the beginning of the loading ramp. For higher levels, the identified values are almost constant for all the image pairs. It is worth noting that the benefit of the regularization is seen with a relatively good stabilization of the identified parameters, especially on Poisson's ratio.

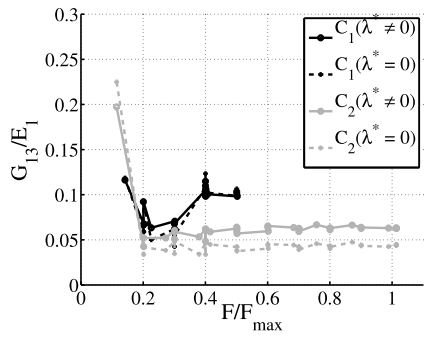
### 5.5. Model Improvement

As explained above, a heterogeneous modeling should improve the description of the material behavior. It is proposed to describe the blade root behavior with four sets of material parameters. The same local orientations are chosen (Figure 4a), but the local orthotropic behavior depends on the regions shown in Figure 20. This partition of the domain has been chosen with respect to the variation of the underlying weaving.

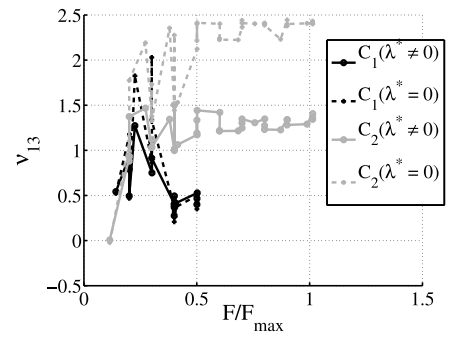
The same regularization procedure is applied to the second loading step, the number of identified parameters is four in each partition  $i = [1, 2, 3, 4]$ , namely,  $\ln(E_1^i/E_{1nom}^1)$ ,  $\ln(E_3^i/E_{1nom}^1)$ ,  $\ln(G_{13}^i/E_{1nom}^1)$ ,  $\nu_{13}^i$ , except for the partition located on the top part of the blade root for which the elastic modulus,  $E_1^1$ , is set to its nominal value. Nominal values are shown in Table 3, and their uncertainties are assumed to be equal to 4%, as previously.

The results shown in Figure 21 are reasonably stable even for this significant number of parameters. The dimensionless residual,  $R_n$  (Figure 21e), is much lower than with the homogeneous description. However, the uncertainties due to acquisition noise (Figure 22) are higher, except for the shear modulus and elastic modulus  $E_3$ . Thus, some parameters cannot be determined. The regularization is necessary to remedy the indeterminacy on these parameters.

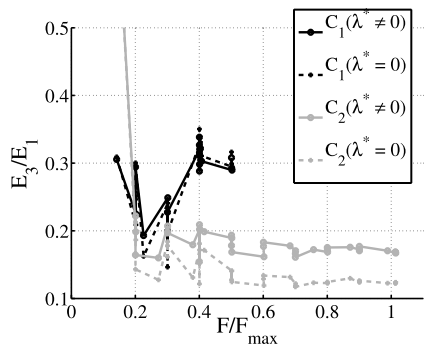
In the present case, the standard deviation of the identification residual  $\sigma_c = 7.3$  gray levels is very close to that of the measurement  $\sigma_c = 6.8$  gray levels and to that of pure noise (*i.e.*,  $\sigma = 5.5$  gray levels). These results are summarized by plotting the histograms of Figure 23b. The quality of the identification is shown by the difference between measured and calculated displacement fields. Figure 23a shows this difference for the image pair 123 – 139. The gain provided by the heterogeneous description is clearly seen, as the residuals are lower than in the homogeneous



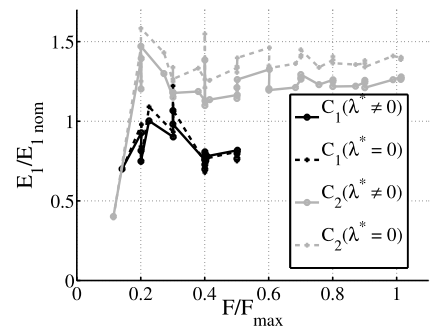
(a)



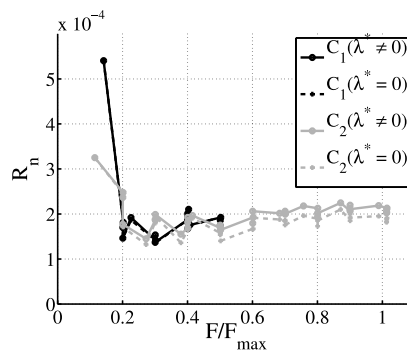
(b)



(c)

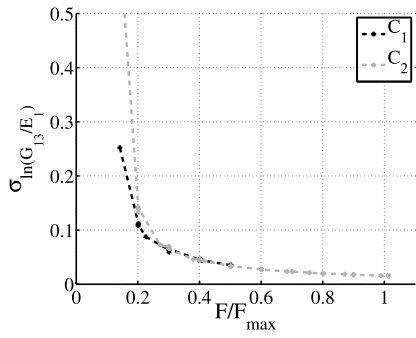


(d)

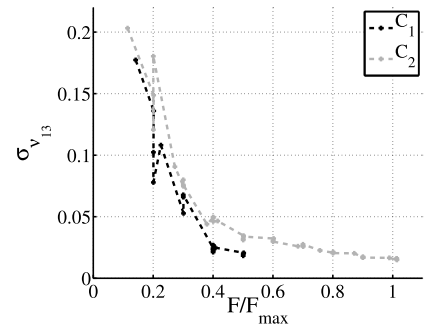


(e)

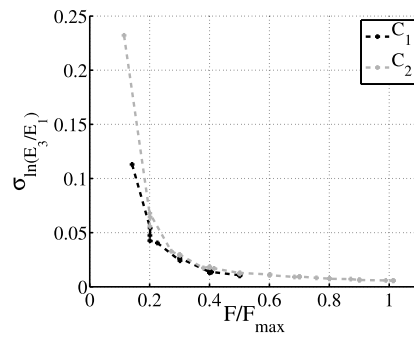
Figure 18: Identified values for the series of images taken during the test vs. applied load. The first (respectively second) ramp is shown in dark (respectively light gray)



(a)



(b)



(c)

Figure 19: Uncertainty values for the series of images taken during the test vs. applied load. The first (respectively second) ramp is shown in dark and labeled  $C_1$  (respectively light gray and labeled  $C_2$ )

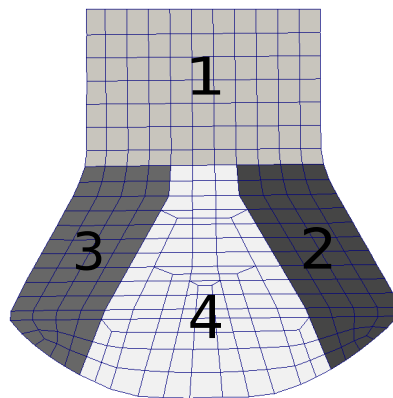
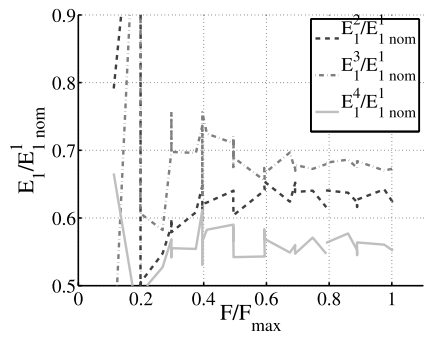
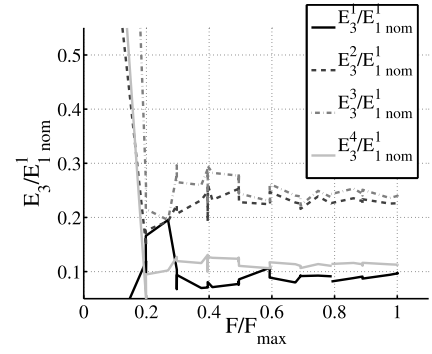


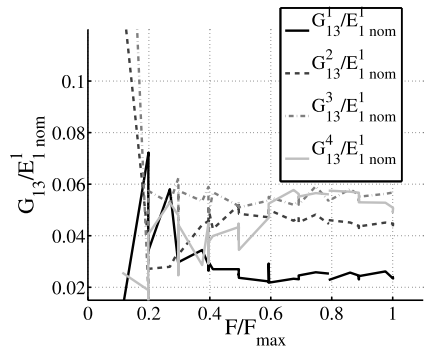
Figure 20: Spatial partitions of local orthotropy where each gray level represents a set of material parameters, numbered from 1 to 4



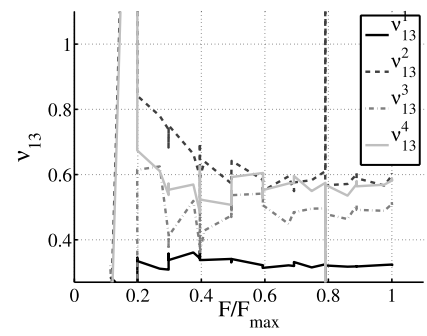
(a)



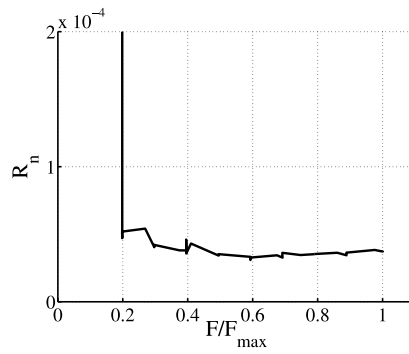
(b)



(c)



(d)

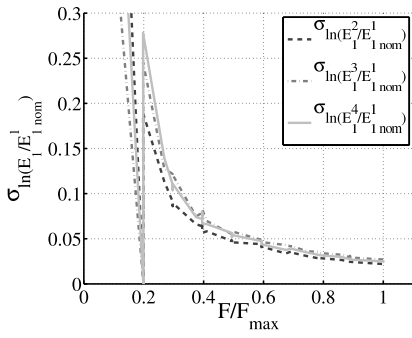


(e)

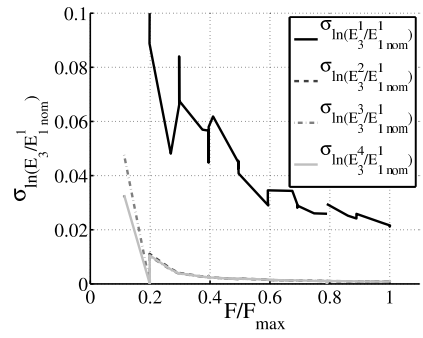
Figure 21: Identified values for the series of images taken during the test on the second loading step vs. applied load for the heterogeneous modeling

Table 3: Nominal values of the different material parameters for each partition  $i$  of the blade root

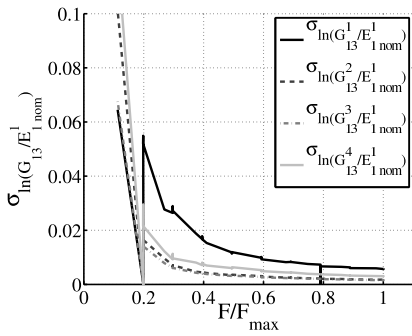
Parameter	Partition			
	i=1	i=2	i=3	i=4
$E_{1nom}^i/E_{1nom}^1$	-	0.645	0.645	0.607
$E_{3nom}^i/E_{1nom}^1$	0.087	0.11	0.11	0.092
$G_{13nom}^i/E_{1nom}^1$	0.037	0.083	0.083	0.055
$\nu_{13nom}^i$	0.38	0.49	0.49	0.47



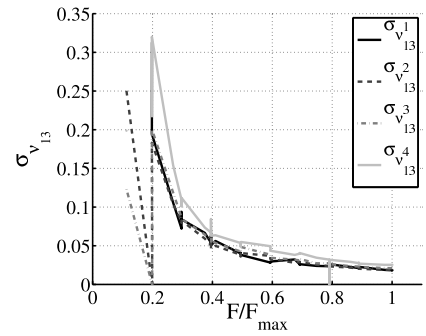
(a)



(b)



(c)



(d)

Figure 22: Uncertainty values for the series of images taken during the test on the second loading step vs. applied load for the heterogeneous modeling

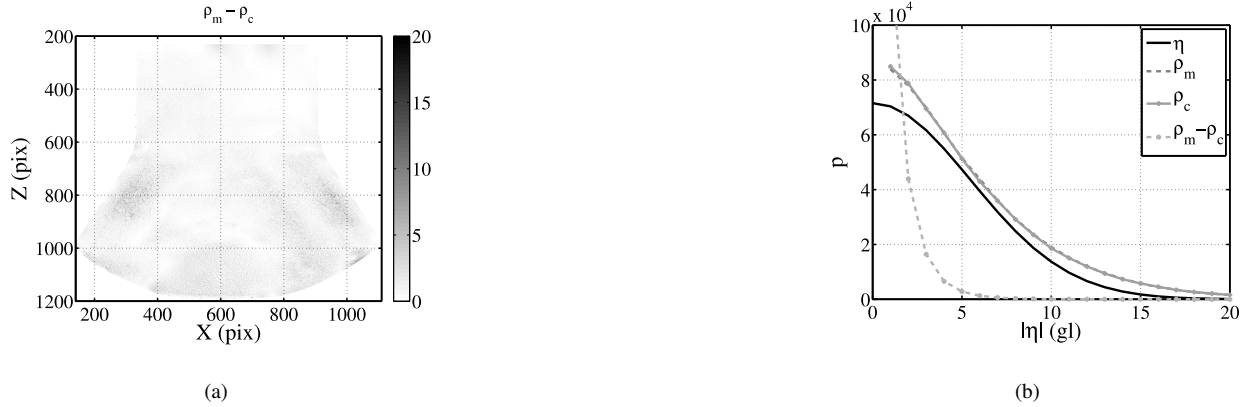


Figure 23: Gray level residuals associated with a measurement and a regularized identification step for the heterogeneous description: (a) difference between measurement residual  $\rho_m$  and identification residual  $\rho_c$ ,  $\rho_m - \rho_c$ . (b) Histograms of gray levels of  $\eta$ ,  $\rho_m$ ,  $\rho_c$ ,  $\rho_m - \rho_c$ . The dynamic range of the reference picture is 1024 gray levels

case, especially in the lower part of the blade root. The heterogeneous description provides a better representation of the behavior of the blade root.

## 6. Conclusion

Working in a unique numerical environment, the global DIC measurement and FEMU identification procedures are performed within a compatible formalism. In particular, an *identical* unstructured mesh adjusted on the actual specimen geometry is utilized. To illustrate the methodology, namely, its performance and limitations, the identification of homogeneous elastic properties of a complex composite part is carried out. It is shown that standard uncertainties resulting from image noise can be related to the identified material properties, and a regularization strategy is implemented to circumvent possible indeterminacy from the considered test (*i.e.*, lack of information to complete the sole identification).

The uncertainty analysis performed herein allows the user to judge from the displacement and gray level residual fields whether the modeling hypothesis is appropriate or if it has the potential to be refined to provide for a more accurate description of the mechanical behavior. For the analyzed example, the residual fields have prompted for such a finer description. However, an automated refinement of the mechanical description is a challenging perspective to the present work.

Another perspective is to resort to integrated (or regularized) approaches to identify material parameters (and boundary conditions) [36]. The present framework combining DIC and FEMU in a single environment is very well adapted to such procedures. In particular, the uncertainty estimates can be assessed by using the same framework as that used herein.

## Acknowledgements

The authors acknowledge the financial support provided by SNECMA (SAFRAN group).

## References

- [1] J. Jewell, R. Kennedy, and A. Menard. CFM Unveils New LEAP-X Engine. *CFM press*, 2008.
- [2] V. A. Guénon, T. W. Chou, and J. W. Gillespie. Toughness properties of a three-dimensional carbon-epoxy composite. *Journal of Materials Science*, 24(11):4168–4175, 1989.
- [3] J. Brandt, K. Drechsler, and F. J. Arendts. Mechanical performance of composites based on various three-dimensional woven-fibre preforms. *Composites Science and Technology*, 56(3):381–386, 1996.
- [4] R. Kamiya, B. A. Cheeseman, P. Popper, and T.-W. Chou. Some recent advances in the fabrication and design of three-dimensional textile preforms: a review. *Composites Science and Technology*, 60(1):33–47, 2000.
- [5] P. Badel, E. Vidal-Sallé, E. Maire, and P. Boisse. Simulation and tomography analysis of textile composite reinforcement deformation at the mesoscopic scale. *Composites Science and Technology*, 68(12):2433–2440, 2008.
- [6] E. De Luycker, F. Morestin, P. Boisse, and D. Marsal. Simulation of 3D interlock composite preforming. *Composite Structures*, 88(4):615–623, 2009.
- [7] D. Durville. Simulation of the mechanical behaviour of woven fabrics at the scale of fibers. *International Journal of Material Forming*, 3(1241):1251, 2010.
- [8] C. El Hage, R. Younès, Z. Aboura, M.L. Benzeggagh, and M. Zoater. Analytical and Numerical Modeling of Mechanical Characteristics of Orthogonal 3D CFRP. In *Proc. 14th JNC*, pages 699–708, 2005.
- [9] S. V. Lomov, G. Perie, D. S. Ivanov, I. Verpoest, and D. Marsal. Modeling three-dimensional fabrics and three-dimensional reinforced composites: challenges and solutions. *Textile Research Journal*, 81(1):28–41, 2011.
- [10] P. Lapeyronnie, P. Le Grogneq, C. Binétruy, and F. Boussu. Homogenization of the elastic behavior of a layer-to-layer angle-interlock composite. *Composite Structures*, 93(11):2795–2807, 2011.
- [11] R. C. Aster, B. Borchers, C.H. Thurber. Parameter estimation and inverse problems. *Academic Press*, 2013.
- [12] B. Weber, P. Paultre, J. Proulx. Structural damage detection using nonlinear parameter identification with Tikhonov regularization. *Structural Control and Health Monitoring*, 14(3):406–427, 2006.
- [13] B. Rahmani, F. Mortazavi, I. Villemure, M. Levesque. A new approach to inverse identification of mechanical properties of composite materials: Regularized model updating. *Composite Structures*, 105(6):116–125, 2013.
- [14] J. Molimard, R. Le Riche, A. Vautrin, J.R. Lee. Identification of the Four Orthotropic Plate Stiffnesses Using a Single Open-hole Tensile Test. *Experimental Mechanics*, 45(5):404–411, 2005.
- [15] A. Moussawi, G. Lubineau, E. Florentin, B. Blaysat. The constitutive compatibility method for identification of material parameters based on full-field measurements. *Computer Methods in Applied Mechanics and Engineering*, 265:1–14, 2013.
- [16] R. Gras, S. Roux, H. Leclerc, J.-N. Périé, S. Otin, and J. Schneider. Identification of out-of-plane shear modulus of a 3D woven composite. *Experimental Mechanics*, 53(5):719–730, 2012.
- [17] M. A. Sutton, J. H. Yan, V. Tiwari, H. W. Schreier, and J. J. Orteu. The effect of out-of-plane motion on 2D and 3D digital image correlation measurements. *Optics and Lasers in Engineering*, 46(10):746–757, 2008.
- [18] S. Buchanan, A. Grigorash, E. Archer, A. McIlhagger, J. Quinn, and G. Stewart. Analytical elastic stiffness model for 3D woven orthogonal interlock composites. *Composites Science and Technology*, 70(11):1597–1604, 2010.

- [19] S. Nehme, A. Hallal, F. Fardoun, R. Younes, B. Hagege, Z. Aboura, M. Benzeggagh, and F. Hage Chehade. Numerical/analytical methods to evaluate the mechanical behavior of interlock composites. *Journal of Composite Materials*, 45(16):1699–1716, 2011.
- [20] G. Besnard, F. Hild, and S. Roux. "Finite-element" displacement fields analysis from digital images : application to Portevin-Le Châtelier bands. *Experimental Mechanics*, 46 :789–804, 2006.
- [21] M. A. Sutton, W. J. Wolters, W. H. Peters, W. F. Ranson, and S. R. McNeill. Determination of displacements using an improved digital correlation method. *Image and Vision Computing*, 1(3):133–139, 1983.
- [22] M. Bornert, F. Brémand, P. Doumalin, J.-C. Dupré, M. Fazzini, M. Grédiac, F. Hild, S. Mistou, J. Molimard, J.-J. Orteu, L. Robert, Y. Surrel, P. Vacher, and B. Wattrisse. Assessment of Digital Image Correlation Measurement Errors: Methodology and Results. *Experimental Mechanics*, 49(3):353–370, 2009.
- [23] H. W. Schreier, J. R. Braasch, and M. A. Sutton. Systematic errors in digital image correlation caused by intensity interpolation. *Optical Engineering*, 39(11):2915–2921, 2000.
- [24] S. Avril, M. Bonnet, A. Bretelle, M. Grédiac, F. Hild, P. Jenny, F. Latourte, D. Lemosse, S. Pagano, E. Pagnacco, and F. Pierron. Overview of Identification Methods of Mechanical Parameters Based on Full-field Measurements. *Experimental Mechanics*, 48(4):381–402, 2008.
- [25] K. T. Kavanagh and R. W. Clough. Finite Element Applications in the Characterization of Elastic Solids. *International Journal of Solids and Structures*, 7(1):11–23, 1971.
- [26] D. Lecompte, A. Smits, H. Sol, J. Vantomme, and D. V. Hemelrijck. Mixed numerical-experimental technique for orthotropic parameter identification using biaxial tensile tests on cruciform specimens. *International Journal of Solids and Structures*, 44(5):1643–1656, 2007.
- [27] S. Roux and F. Hild. Stress intensity factor measurements from digital image correlation: post-processing and integrated approaches. *International Journal of Fracture*, 140(1):141–157, 2006.
- [28] E.J.J. Van Campen. Parameter Identification of the Orthotropic Material Wood. Master's thesis, Universiteit Eindhoven, <http://alexandria.tue.nl/repository/books/628249.pdf>, April 1992.
- [29] H. Leclerc. Nouveaux outils de mécanique et d'analyse numérique pour le LMT. Séminaire du LMT Cachan. <http://www.lmt.ens-cachan.fr/seminaire/transparentes/leclerc-transparentes.pdf>, 2005.
- [30] H. Leclerc. Plateforme metil : optimisations et facilités liées à la génération de code. Colloque National en Calcul des Structures, Giens, 2007.
- [31] J. Réthoré and M. François. Curve and boundaries measurement using B-splines and virtual images. *Optics and Lasers in Engineering*, 52(1):145-155, 2014.
- [32] J. Réthoré. A fully integrated noise robust strategy for the identification of constitutive laws from digital images. *International Journal for Numerical Methods in Engineering*, 84(6):631–660, 2010.
- [33] H. Leclerc, J.-N. Périé, S. Roux, and F. Hild. Voxel-Scale Digital Volume Correlation. *Experimental Mechanics*, 51(4):479–490, 2011.
- [34] F. Hild and S. Roux. Comparison of Local and Global Approaches to Digital Image Correlation. *Experimental Mechanics*, 52(9):1503–1519, 2012.
- [35] G. Huysmans, I. Verpoest, and P. Van Houtte. A poly-inclusion approach for the elastic modelling of knitted fabric composites. *Acta Materialia*, 46(9):3003–3013, MAY 22 1998.
- [36] H. Leclerc, J.-N. Périé, S. Roux, and F. Hild. Integrated Digital Image Correlation for the Identification of Mechanical Properties. In *Computer Vision/Computer Graphics Collaboration Techniques*, pages 161–171. Springer Berlin / Heidelberg, 2009.